Backbone Transitions and Invariant Tori in Forced Micromechanical Oscillators with Optical Detection

Tuhin Sahai[a,b]

a) currently at United Technologies Research Center, 411 Silver Lane MS 129-85, East Hartford, CT 06108

February 5, 2010

Abstract

Micromechanical oscillators often display rich dynamics due to nonlinearities in their response, actuation and detection. This paper investigates the complicated response of a forced micromechanical oscillator. In particular, we investigate a thermally induced transition in the resonant response of a forced micromechanical oscillator with optical detection; and the branch of invariant tori formed at subsequent bifurcations that occur with increasing laser power. We use perturbation theory and continuation algorithms to investigate and compute branches of invariant tori. The results of both methods are compared.

1   Introduction

Micromechanical oscillators have become an active area of research in the last few years. With numerous applications in sensing [1, 2, 3, 4], signal processing [5], clock generation [6], pattern recognition [7] and computer memory [8] to name a few. Micro systems display a wide range of nonlinear behavior seen rarely in the macro world [9, 10, 11, 12, 13, 14]. In this paper we investigate the details of a transition in the response of a forced micro-oscillator along with resulting branches of invariant tori (quasiperiodic motion). This paper demonstrates (by example) how simple micro-systems can display complicated dynamics. It is important to understand the subtle behavior of these systems (using experimental and numerical means) before using them for myriad applications. The dynamics, once well understood can be exploited for appropriate applications.

In Ref. [15] we demonstrated and explained a peculiar softening hardening transition in the resonant response of a doubly clamped micro-oscillator, with piezo forcing and optical detection (see Fig. 1) It was experimentally found that on increasing the incident laser power (meant for motion detection), the resonant response of the beam changes from softening to hardening (all other parameters were held constant). Figs. 2 and 3 show the (numerically computed) softening to hardening transition. For the transition observed in experiments please see [15]. This transition turns out to be a consequence of subtle interplay between the temperature dependence of the linear and cubic stiffnesses of the oscillator. The oscillator

1

a

b

Figure 1: a) SEM image of top view of the paddle oscillator b) Schematic of the experimental setup
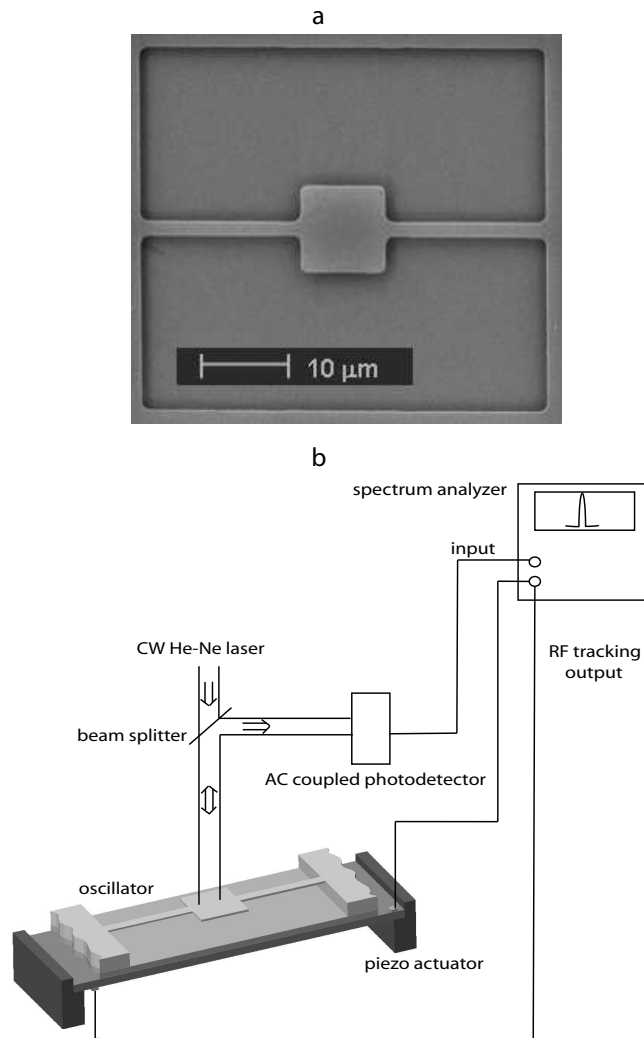
is under tension ($\approx$ 50MPa) due to the fabrication procedure [15]. At low laser power the expansion due to heating is lower, so the initial tension in the system is higher making the effect of the cubic stiffness negligible (since the cubic stiffness is a result of induced tension in the beam due to deflection). Also, the linear stiffness has negative dependence on temperature, whereas, the cubic stiffness has positive dependence on temperature (Eqn. 1: for derivations see [15]). On increasing laser power the softening to hardening transition occurs due to a competition between the linear and cubic terms. The linear stiffness wins at low laser power (Figs. 2(a) and 3(a)), while cubic wins at high laser power (Figs. 2(d) and 3(d)). At intermediate laser power we find that the resonant response has the characteristics of both softening and hardening resonances (Figs. 2(b), 3(b), 2(c) and 3(c)). For more details about modeling of the oscillator see [15].

The equations used to model the oscillator are [15]:

$$\ddot{z} + \frac{\dot{z}}{Q} + (1 + cT)z + (1 + b_1 T + b_2 T^2 + b_3 T^3)\beta z^3 = F_s \sin(\omega t), \qquad (1)$$

$$\dot{T} = -BT + HP(\alpha + \gamma \sin^2(2\pi(z - z_i))),$$

where z and T are normalized deflection and temperature above ambient. The values of parameters in the equations are $Q \approx 1400$, $c = -0.011/K$, $b_1 = 1.37 \times 10^{-2}I/K$, $b_2 = 2 \times 10^{-6}1/K^2$, $b_3 = 2 \times 10^{-5}1/K^3$, $\beta = 0.875$ and $F_s = 5 \times 10^{-5}$; $H = 2.99 \times 10^{-2}\frac{K}{\mu W}$, $B = 4 \times 10^{-3}$ (dimensionless), $\alpha \approx 1.325 \times 10^{-1}$, $\gamma \approx 8.4 \times 10^{-2}$ and $z_i \approx 5 \times 10^{-2}$ [15]. We use continuation algorithms [16, 17] to compute resonant responses at different laser powers (parameter P in Eqn. 1), shown in Fig. 2 and 3. We find that at higher laser power the oscillator loses stability at torus bifurcations. Unfortunately we cannot compute the branch of invariant tori using standard continuation software, so as a first approximation we can compute the branch using simple ODE integration. This gives us the branch of invariant tori in Fig. 2 and 3 and we can predict the locations of jumps and drops in the resonant response on sweeping in frequency [15]. We find that in Figs. 2(b) and 3(b) the torus is born at one torus bifurcation and dies at the other torus bifurcation. At higher laser power (Figs. 2(c), 3(c), 2(d) and 3(d)) the invariant torus (on sweeping in ω) disappears. This causes a jump from the branch of tori to the top of the resonance curve (see Figs. 2(c), 2(d), 3(c) and 3(d)). It is important to note that, these stable aperiodic orbits will be missed experimentally since the system responds at a combination of frequencies one of which is the driving frequency, and the other is close to the natural frequency of the linear oscillator. The spectrum analyzer detects output in a very narrow band around the driving frequency, thus completely missing the second frequency. These numerical results do not give us any insight into the reasons of the disappearance of the branch of invariant tori that gives rise to the jumps and drops. In this paper we will try and analyze this transition and the branches of invariant tori in more detail along with the ensuing bifurcations.

2 Perturbation Analysis

We first use perturbation analysis to try and capture the overall picture presented in Fig. 2 and 3. This includes the thermally induced transitions as well as the invariant tori that are

3

(a) Softening at low laser power ($P = 20\mu W$)

(b) Transition from softening ($P = 22\mu W$)

(c) Transition to hardening ($P = 60\mu W$)

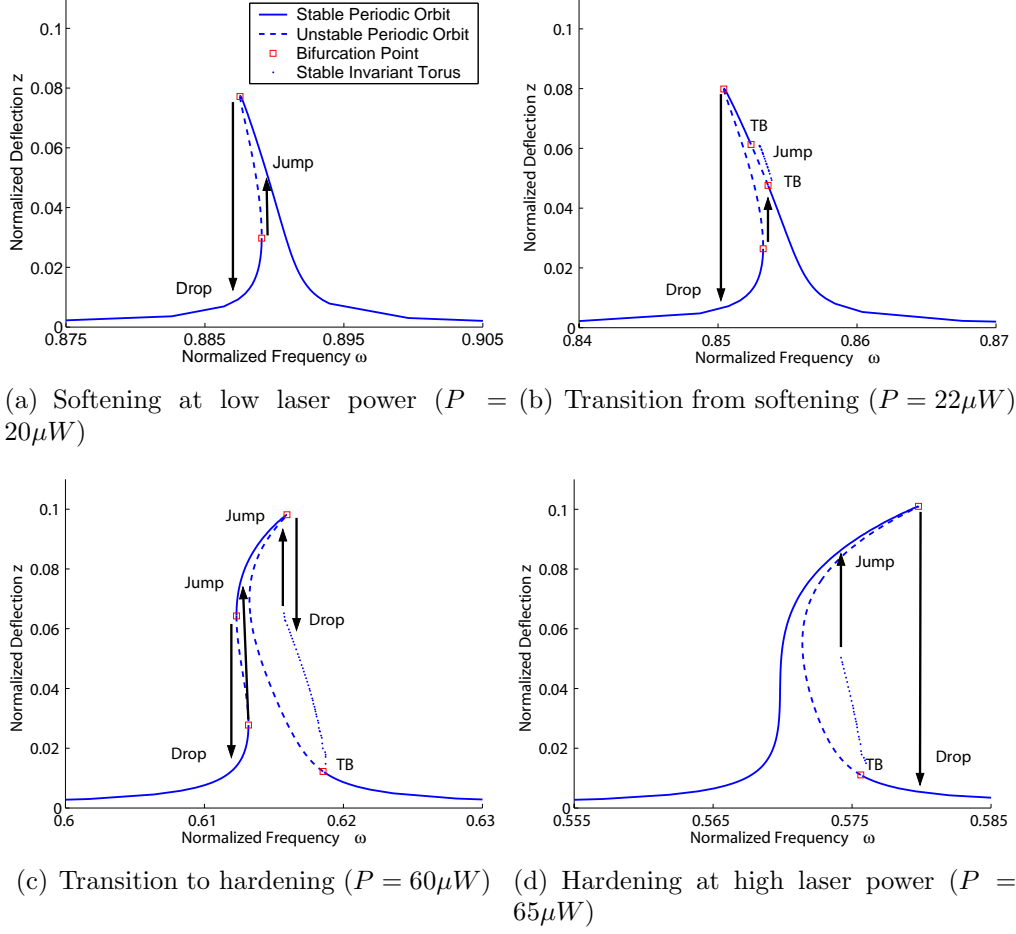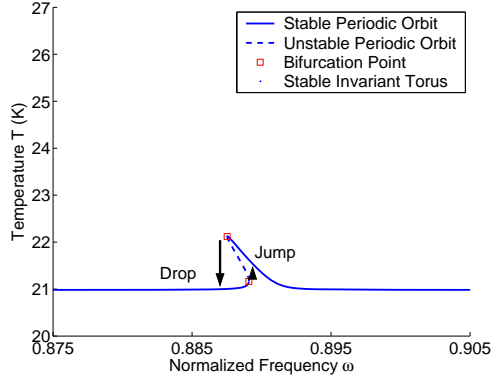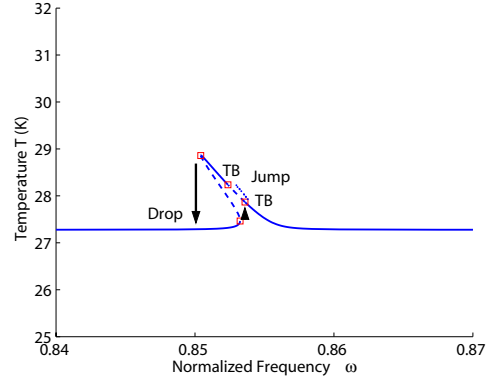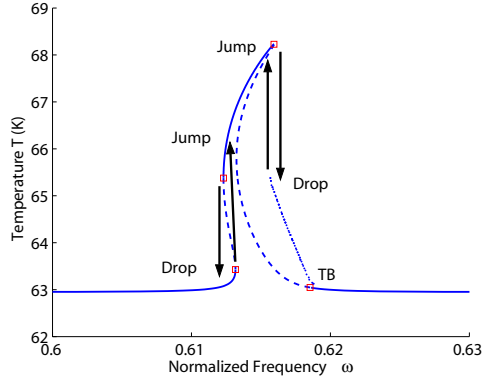(d) Hardening at high laser power ($P = 65\mu W$)

Figure 2: Maximum deflection vs. frequency at various laser powers. Solid lines denote stable periodic orbits, dotted lines denote unstable periodic orbits, open squares denote bifurcation points and dots denote stable invariant tori. TB: Torus Bifurcation
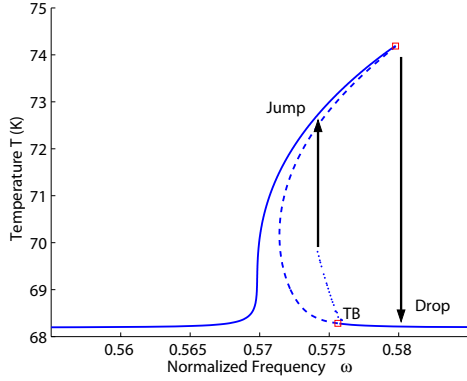
4

(a) Softening at low laser power ($P = 20\mu W$)

(b) Transition from softening ($P = 22\mu W$)

(c) Transition to hardening ($P = 60\mu W$)

(d) Hardening at high laser power ($P = 65\mu W$)

Figure 3: Maximum temperature vs. frequency at various laser powers. Solid lines denote stable periodic orbits, dotted lines denote unstable periodic orbits, open squares denote bifurcation points and dots denote stable invariant tori. TB: Torus Bifurcation

born at torus bifurcations. For this task we use the method of multiple scales [18, 19, 20]. We first perform the perturbation analysis to $O(\epsilon)$, find that it is inadequate, and then go to $O(\epsilon^2)$.

2.1 Multiple Scales to $O(\epsilon)$

Method of multiple scales [18] is based on the assumption that the system dynamics inherently has multiple time scales (two for an expansion to $O(\epsilon)$). For expansions upto $O(\epsilon)$ these scales would naturally be the time scale that involves the periodic solution or stretched time given by $\xi = \omega t$; and the time of approach to the periodic solution or slow time $\eta = \epsilon t$. Here ω is the forcing frequency or frequency of the piezo drive. We assume that parameters β, M, $\frac{1}{Q}$ and γ are $O(\epsilon)$. This assumption is made so that the governing equation (Eqn. 1) to $O(1)$ is a simple harmonic oscillator. The result of this approach is a set of ODEs for the dynamics of the oscillator in the Poincaré section. Thus, periodic solutions become fixed points, torus bifurcations become Hopf bifurcations and, consequently, invariant tori become limit cycles. The time derivatives become:

$$\frac{d}{dt} = \frac{d\xi}{dt}\frac{\partial}{\partial\xi} + \frac{d\eta}{dt}\frac{\partial}{\partial\eta}$$
$$= \omega\frac{\partial}{\partial\xi} + \epsilon\frac{\partial}{\partial\eta}$$

$$\frac{d^2}{dt^2} = \omega^2\frac{\partial^2}{\partial\xi^2} + 2\omega\epsilon\frac{\partial^2}{\partial\xi\partial\eta} + \epsilon^2\frac{\partial^2}{\partial\eta^2} \tag{2}$$

The assumption of M, β, γ and $\frac{1}{Q}$ being $O(\epsilon)$ gives

$$\ddot{z} + \epsilon\frac{\dot{z}}{Q'} + (1 + cT)z + \epsilon(1 + b_1T + b_2T^2 + b_3T^3)\beta' z^3 = \epsilon M' \sin(\omega t), \tag{3}$$

$$\dot{T} + BT = HP(\alpha + \epsilon\gamma' \sin^2(2\pi(z - z_i))), \tag{4}$$

where $Q' = \epsilon Q$, $\beta' = \frac{\beta}{\epsilon}$, $M' = \frac{M}{\epsilon}$ and $\gamma' = \frac{\gamma}{\epsilon}$ (we assume Q', β', M' and γ' are constants). Substituting $\epsilon = 0$ into the equations and dropping the superscripts $'$ for convenience gives the following equation,

$$\ddot{z} + (1 + cT)z = 0, \tag{5}$$

$$\dot{T} + BT = HP\alpha. \tag{6}$$

We expand the normalized displacement and temperature above ambient as a series in ϵ,

$$z = z_0(\xi, \eta) + \epsilon z_1(\xi, \eta) + O(\epsilon^2),$$
$$T = T_0(\xi, \eta) + \epsilon T_1(\xi, \eta) + O(\epsilon^2). \tag{7}$$

The forcing frequency ω is assumed to be close to the natural frequency ω_0 of the oscillator given by [21],

$$\omega^2 = \omega_0^2 + \epsilon\sigma + O(\epsilon^2), \tag{8}$$

6

where $\omega_0 = \sqrt{1 + cT_0(\xi, \eta)}$. This implies that,

$$\omega = \omega_0 + \epsilon \frac{\sigma}{2\omega_0} + \ldots \tag{9}$$

In Eqn. 9 let $k_1 = \frac{\sigma}{2\omega_0}$ making,

$$\omega = \omega_0 + \epsilon k_1, \tag{10}$$

to $O(\epsilon)$. Substituting Eqns. 2, 7, 10 into Eqn. 4 gives,

$$\omega_0 \frac{\partial T(\xi, \eta)}{\partial \xi} - BT_0(\xi, \eta) = HP,$$

$$\omega_0^2 \frac{\partial^2 z_0(\xi, \eta)}{\partial \xi^2} + (1 + cT_0(\xi, \eta))z_0(\xi, \eta) = 0. \tag{11}$$

The solution of the above equation is,

$$T_0(\xi, \eta) = \frac{HP}{B},$$

$$z_0(\xi, \eta) = X(\eta)\cos(\xi) + Y(\eta)\sin(\xi), \tag{12}$$

where $X(\eta)$ and $Y(\eta)$ are slowly varying coefficients. We expand the $\sin^2(2\pi(z - z_i))$ term as a Taylor series of the form,

$$\sin^2(2\pi(z - z_i)) \approx 4\pi^2(z - z_i)^2 + h.o.t. \tag{13}$$

Taking more terms in the above expansion is found to make no qualitative difference to the results. We now substitute the solution obtained for z_0 and T_0 into the first order equations ($O(\epsilon)$ equations) given by,

$$\omega_0 \frac{\partial T_1(\xi, \eta)}{\partial \xi} + BT_1(\xi, \eta) - 4HP\gamma\pi^2(z_0(\xi, \eta) - z_i)^2 = 0, \tag{14}$$

$$\omega_0 \frac{\partial^2 z_1(\xi, \eta)}{\partial \xi^2} + 2\omega_0 \frac{\partial^2 z_0(\xi, \eta)}{\partial \xi \partial \eta} + 2\omega_0 k_1 \frac{\partial^2 z_0(\xi, \eta)}{\partial \xi^2} + \frac{\omega_0}{Q} \frac{\partial z_0(\xi, \eta)}{\partial \xi} + (1 + cT_0(\xi, \eta))z_1(\xi, \eta)$$

$$+cT_1(\xi, \eta)z_0(\xi, \eta) - M\sin(\xi) + (1 + b_1 T_0(\xi, \eta) + b_2 T_0(\xi, \eta)^2 + b_3 T_0(\xi, \eta)^3)\beta z_0(\xi, \eta)^3 = 0. \tag{15}$$

The particular solution of $T_1(\xi, \eta)$ is assumed to be of the form,

$$T_1(\xi, \eta) = p_1(\eta) + p_2(\eta)\sin(\xi) + p_3(\eta)\cos(\xi) + p_4(\eta)\sin(2\xi) + p_5(\eta)\cos(2\xi). \tag{16}$$

We substitute Eqn. 16 into Eqn. 14 and solve for the coefficients $p_i(\eta)$. Using the solution for $T_1(\xi, \eta)$ in Eqn. 15 we get,

$$\omega_0^2 \frac{\partial^2 z_1(\xi, \eta)}{\partial \xi^2} + (1 + cT_0(\xi, \eta))z_1(\xi, \eta) = (\ldots)\sin(\xi) + (\ldots)\cos(\xi) + \text{non-secular terms.} \tag{17}$$

7

Setting the coefficients of $\sin(\xi)$ and $\cos(\xi)$ (the equations in (...)) to zero, gives the resulting slow flow equations to $O(\epsilon)$,

$$
\begin{aligned}
\frac{dX(\eta)}{d\eta} &= a_1 X(\eta) + a_2 X(\eta)^3 + a_3 X(\eta)Y(\eta)^2 + a_4 X(\eta)^2 Y(\eta) + a_5 Y(\eta)^3 + a_6 Y(\eta) \\
&\quad + k_1 Y(\eta), \\
\frac{dY(\eta)}{d\eta} &= a_1 Y(\eta) + a_2 Y(\eta)^3 + a_3 X(\eta)^2 Y(\eta) - a_4 X(\eta)Y(\eta)^2 - a_5 X(\eta)^3 - a_6 X(\eta) \\
&\quad - k_1 X(\eta) - M_1.
\end{aligned}
\tag{18}
$$

Different values of P give different coefficients in the above equation (Eqn. 18). In the next section we vary the value of P and analyze the predictions using continuation on Eqn. 18.

2.1.1 Results

AUTO 2000 [16, 17] is used to perform continuation on Eqn. 18. k_1 is used as a continuation parameter. We compute the resonance curves for different laser powers (different values of P). The initial point for continuation is obtained by setting $k_1 = 0$, $\frac{dX(\eta)}{d\eta} = 0$ and $\frac{dY(\eta)}{d\eta} = 0$ and solving for X and Y using a numerical root finder. We then sweep in k_1 (detuning) to find the entire branch of equilibria.

The results obtained from continuation (using AUTO 2000) can be found in Fig. 4. The x-axis in Fig. 4 is k_1 and y-axis is $R = \sqrt{X(\eta)^2 + Y(\eta)^2}$. Fig. 4(a) shows a softening response. On increasing the laser power, the response looks like the Lorentzian response of a simple harmonic oscillator (Fig. 4(b)). On increasing the laser power further, the response becomes hardening Fig. 4(c). We find that the transition from softening to hardening is captured (as seen in Fig. 4), though the torus bifurcations are not. All the bifurcations in Fig. 4 are saddle-nodes.

To predict the torus bifurcation and study the branches of tori in Fig. 2 we go one order higher in our perturbation calculation. Due to the approximation involved in our perturbation calculation, the laser power value at which the softening-hardening transition occurs has changed slightly (see Fig. 2).
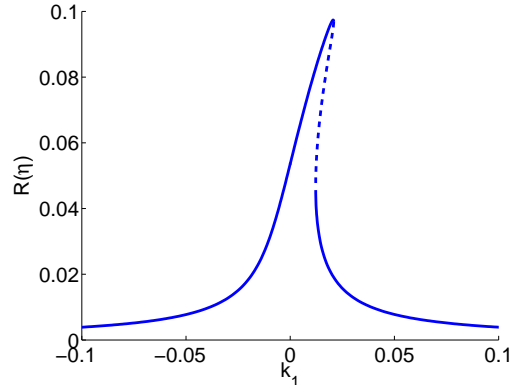
2.2 Multiple Scales to $O(\epsilon^2)$

To go to $O(\epsilon^2)$ we need to add another time scale to our calculation, $\psi = \epsilon^2 t$. So the first order derivative becomes,

$$
\begin{aligned}
\frac{d}{dt} &= \frac{d\xi}{dt}\frac{\partial}{\partial \xi} + \frac{d\eta}{dt}\frac{\partial}{\partial \eta} + \frac{d\psi}{dt}\frac{\partial}{\partial \psi}, \\
&= \omega\frac{\partial}{\partial \xi} + \epsilon\frac{\partial}{\partial \eta} + \epsilon^2\frac{\partial}{\partial \psi}.
\end{aligned}
\tag{19}
$$

The second order derivatives can be obtained by operating Eqn. 19 onto itself and neglecting terms of $O(\epsilon^3)$. We do not change the rescaling done in Eqn. 4. Expansion of terms in Eqn. 7
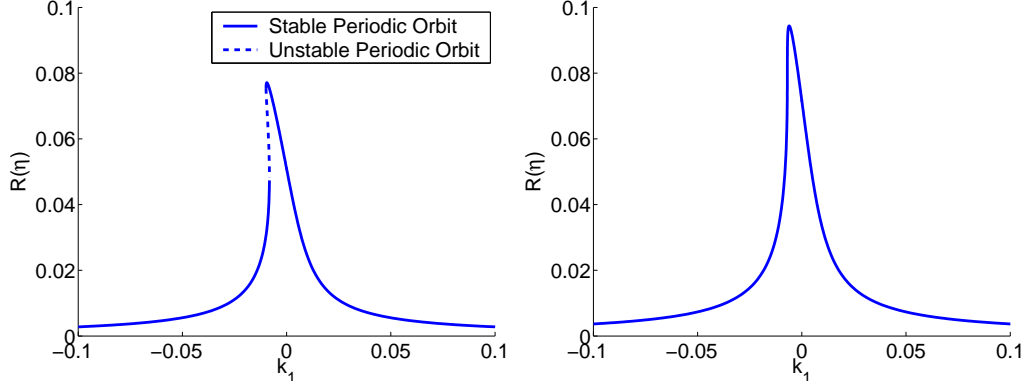
(a) Softening at low laser power $(P = 20\mu W)$

(b) Transition from softening $(P = 30\mu W)$

(c) Transition to hardening $(P = 40\mu W)$

Figure 4: Perturbation results (using multiple scales) for $O(\epsilon)$. The transition from softening to hardening is captured. The torus bifurcation (and the subsequent branch of invariant tori) is not captured.

now becomes,

$$z = z_0(\xi,\eta,\psi) + \epsilon z_1(\xi,\eta,\psi) + \epsilon^2 z_2(\xi,\eta,\psi) + O(\epsilon^3),$$
$$T = T_0(\xi,\eta,\psi) + \epsilon T_1(\xi,\eta,\psi) + \epsilon^2 T_2(\xi,\eta,\psi) + O(\epsilon^3). \tag{20}$$

The expansion for ω now becomes [21],

$$\omega = \omega_0 + \epsilon k_1 - \epsilon^2 \frac{k_1^2}{2\omega_0} + O(\epsilon^3), \tag{21}$$

The $O(\epsilon)$ slow flow equations remain the same. $X(\eta)$ becomes $X(\eta,\psi)$ and $Y(\eta)$ becomes $Y(\eta,\psi)$ in Eqn. 12. Also, since p_i's in Eqn. 16 are functions of $X(\eta,\psi)$ and $Y(\eta,\psi)$, they too become functions of η and ψ. The slow flow equations to $O(\epsilon)$ now have the form,

$$\frac{dX(\eta,\psi)}{d\eta} = a_1 X(\eta,\psi) + a_2 X(\eta,\psi)^3 + a_3 X(\eta,\psi) Y(\eta,\psi)^2 + a_4 X(\eta,\psi)^2 Y(\eta,\psi)$$

$$+ a_5 Y(\eta,\psi)^3 + a_6 Y(\eta,\psi) + k_1 Y(\eta,\psi),$$

$$\frac{dY(\eta,\psi)}{d\eta} = a_1 Y(\eta,\psi) + a_2 Y(\eta,\psi)^3 + a_3 X(\eta,\psi)^2 Y(\eta,\psi) - a_4 X(\eta,\psi) Y(\eta,\psi)^2$$

$$- a_5 X(\eta,\psi)^3 - a_6 X(\eta,\psi) - k_1 X(\eta,\psi) - M_1. \tag{22}$$

We will now compute $\frac{X(\eta,\psi)}{d\psi}$ and $\frac{Y(\eta,\psi)}{d\psi}$, and add the equations (i.e. $\frac{dX(\eta,\psi)}{d\eta} + \epsilon \frac{X(\eta,\psi)}{d\psi}$ and $\frac{dY(\eta,\psi)}{d\eta} + \epsilon \frac{Y(\eta,\psi)}{d\psi}$), by method of reconstitution [21] to get the slow flow equations to $O(\epsilon^2)$ [19, 20, 22].

To get $\frac{X(\eta,\psi)}{d\psi}$ and $\frac{Y(\eta,\psi)}{d\psi}$ we need to get the solution to Eqn. 17. The secular terms in the equations have now been set to zero, so we look for solutions to $z_1(\eta,\psi)$ of the form,

$$z_1(\xi,\eta,\psi) = q_1(\eta,\psi) + q_2(\eta,\psi)\sin(\xi) + q_3(\eta,\psi)\cos(\xi) + q_4(\eta,\psi)\sin(2\xi)$$

$$+ q_5(\eta,\psi)\cos(2\xi) + q_6(\eta,\psi)\sin(3\xi) + q_7(\eta,\psi)\cos(3\xi). \tag{23}$$

The complementary part of Eqn. 17 is neglected since we are not solving a specific initial value problem [23] (even if we were, the initial condition could be satisfied by the entire solution i.e. $O(1) + O(\epsilon) + O(\epsilon^2) + \dots$ [22]). We then substitute the solution obtained for $z_1(\xi,\eta,\psi)$ into the temperature equation and collect terms of $O(\epsilon^2)$. The temperature equation to $O(\epsilon^2)$ is,

$$\omega_0 \frac{\partial T_2(\xi,\eta,\psi)}{\partial\xi} + \frac{\partial T_1(\xi,\eta,\psi)}{\partial\eta} + k_1 \frac{\partial T_1(\xi,\eta,\psi)}{\partial\xi} + BT_2(\xi,\eta,\psi)$$

$$- 8AP\gamma\pi^2 z_1(\xi,\eta,\psi)(z_0(\xi,\eta,\psi) - z_i) = 0. \tag{24}$$

We again find the particular solution for $T_2(\xi,\eta,\psi)$ of the form,

$$T_2(\xi,\eta,\psi) = r_1(\eta,\psi) + r_2(\eta,\psi)\sin(\xi) + r_3(\eta,\psi)\cos(\xi) + r_4(\eta,\psi)\sin(2\xi)$$

$$+ r_5(\eta,\psi)\cos(2\xi) + r_6(\eta,\psi)\sin(3\xi) + r_7\cos(3\xi) + r_8(\eta,\psi)\sin(4\xi) + r_9(\eta,\psi)\cos(4\xi). \tag{25}$$

10

We now substitute the solutions for $z_0(\xi, \eta, \psi)$, $T_0(\xi, \eta, \psi)$, $z_1(\xi, \eta, \psi)$, $T_1(\xi, \eta, \psi)$ and $T_2(\xi, \eta, \psi)$ into Eqn. 4 and collect $O(\epsilon^2)$ terms. The resulting equation is similar to Eqn. 17,

$$\omega_0^2 \frac{\partial^2 z_2(\xi, \eta, \psi)}{\partial \xi^2} + (1 + cT_0(\xi, \eta, \psi))z_2(\xi, \eta, \psi) = (\ldots)\sin(\xi) + (\ldots)\cos(\xi)$$

$$+ \quad \text{non-secular terms.} \qquad (26)$$

Putting the coefficients of $\sin(\xi)$ and $\cos(\xi)$ to zero, we get relations for $\frac{\partial X(\eta, \psi)}{\partial \psi}$ and $\frac{\partial Y(\eta, \psi)}{\partial \psi}$ of the form,

$$\frac{dX(\eta, \psi)}{d\psi} = \sum_{i=0}^{5} b_i X(\eta, \psi)^i Y(\eta, \psi)^{5-i} + k_2 Y(\eta, \psi) - M_2,$$

$$\frac{dY(\eta, \psi)}{d\psi} = \sum_{i=0}^{5} c_i X(\eta, \psi)^i Y(\eta, \psi)^{5-i} - k_2 X(\eta, \psi) - M_3. \qquad (27)$$

Here some of the b_i's and c_i's are functions of k_1. As mentioned earlier, to finally get the slow flow relations to $O(\epsilon^2)$ we add terms from the different time scales $\frac{dX(\eta, \psi)}{d\eta} + \epsilon \frac{dX(\eta, \psi)}{d\psi}$ and $\frac{dY(\eta, \psi)}{d\eta} + \epsilon \frac{dY(\eta, \psi)}{d\psi}$ which gives,

$$\frac{dX(\eta, \psi)}{d\eta} + \epsilon \frac{dX(\eta, \psi)}{d\psi} = a_1 X(\eta, \psi) + a_2 X(\eta, \psi)^3 + a_3 X(\eta, \psi)Y(\eta, \psi)^2$$

$$+a_4 X(\eta, \psi)^2 Y(\eta, \psi) + a_5 Y(\eta, \psi)^3 + a_6 Y(\eta, \psi) + k_1 Y(\eta, \psi)$$

$$+\epsilon(\sum_{i=0}^{5} b_i X(\eta, \psi)^i Y(\eta, \psi)^{5-i} + k_2 Y(\eta, \psi) - M_2)$$

$$\frac{dY(\eta, \psi)}{d\eta} + \epsilon \frac{dY(\eta, \psi)}{d\psi} = a_1 Y(\eta, \psi) + a_2 Y(\eta, \psi)^3 + a_3 X(\eta, \psi)^2 Y(\eta, \psi)$$

$$-a_4 X(\eta, \psi)Y(\eta, \psi)^2 - a_5 X(\eta, \psi)^3 - a_6 X(\eta, \psi) - k_1 X(\eta, \psi) - M_1$$

$$+\epsilon(\sum_{i=0}^{5} c_i X(\eta, \psi)^i Y(\eta, \psi)^{5-i} - k_2 X(\eta, \psi) - M_3) \qquad (28)$$

As before (to $O(\epsilon)$), coefficients in the slow flow equations (Eqn. 28) are functions of P. Now that we have the slow flow relations to $O(\epsilon^2)$ we again use continuation algorithms (AUTO 2000) to analyze them for different values of laser power P.

2.2.1 Results

For low laser power we find the same softening response that was seen in the original model (Fig. 2(a)). On increasing laser power we find the same bifurcations in Fig. 5(b) that were seen previously in Fig. 2(b). Since the slow flow reduces torus bifurcations to Hopf bifurcations, we can now use AUTO 2000 to track the limit cycles. In Fig. 5(b) we find that the limit cycles are born at a Hopf bifurcation and eventually die at the other Hopf bifurcation (this is similar to the case in Fig. 2(c)). On increasing laser power, the resonance response begins to show a hardening response, seen in Fig. 5(c) (qualitatively the same as

11

Fig. 2(c)). The limit cycle born at the Hopf bifurcation (example shown Fig. 6) dies at a bifurcation where the time period diverges (shown in Fig. 7), making homoclinic or infinite period bifurcations the most likely candidates [24]. The limit cycle collides with the fixed points very close to the saddle node bifurcation at the top of the resonance curve, shown in Fig. 8. It is found by computing the stability of the fixed points that this bifurcation is an infinite period bifurcation. On increasing laser power we get the pure hardening response in Fig. 5(d) (qualitatively same as Fig. 2(d)). The limit cycle born at the Hopf in this case loses stability through a saddle node bifurcation following which the time period starts to diverge (Fig. 9), again at an infinite period bifurcation bifurcation. A phase portrait of the slow flow equations shows that at the bifurcation point saddle connections (formed by the colliding limit cycle) exist between the saddle point and stable equilibrium (Fig. 10). It is important to note that there is no scenario in which only unstable equilibria exist in phase space. Stable solutions always coexist with unstable equilibria (i.e. there always exists a stable attractor in the system). The results from multiple scales do not match numerical integration (see Figs. 2 and 3) as we may have extended the method of multiple scales beyond the range of validity [21]. It is possible that the rescaling of variables in Eqns. 3 and 4 is itself not valid. In other words, perturbing off a simple harmonic oscillator is not a good assumption. The mismatch could also be a consequence of spurious solutions introduced by the softening effect of the thermal part of the stiffnesses [21]. An expansion to $O(\epsilon^3)$ may give more accurate results. To compute the branch of invariant tori more accurately we now use continuation techniques.

3   Continuation of Invariant Tori

A number of numerical algorithms to approximate quasiperiodic orbits have been developed over the years. Chua and Ushida [25] generalized harmonic balance used for the approximation of periodic orbits, to a spectral balance method for the approximation of quasiperiodic orbits. Fourier polynomials are used to represent the quasiperiodic signal. The basis has to be judiciously chosen to avoid a small divisor problem. Díez, Jorba and Simó [26] have independently developed a similar approach.

Another approach by Schilder et al [27] is based on a graph transform method. They propose a parametrization of the invariant torus. Using the fact that the vector field is tangential to the surface of the torus, they obtain an invariance condition (a first order PDE). To fix the arbitrary phases of the torus they derive a phase condition in a manner very similar to the conditions derived in AUTO 97 to track limit cycles [28]. In this work we implement the algorithm proposed by I. G. Kevrekidis et al [29]. This algorithm essentially reduces the problem of computing invariant tori to a Newton iteration of a functional equation. We pick this approach due to ease of implementation and quadratic convergence independent of flow properties around the torus [29].

3.1   Numerical Method

The algorithm [29] computes invariant curves in the Poincaré section with changing parameter, by transforming the functional equation into a large system of nonlinear equations.

(a) Softening at low laser power ($P = 20\mu W$)

(b) Transition from softening ($P = 40\mu W$)

(c) Transition to hardening ($P = 65\mu W$)
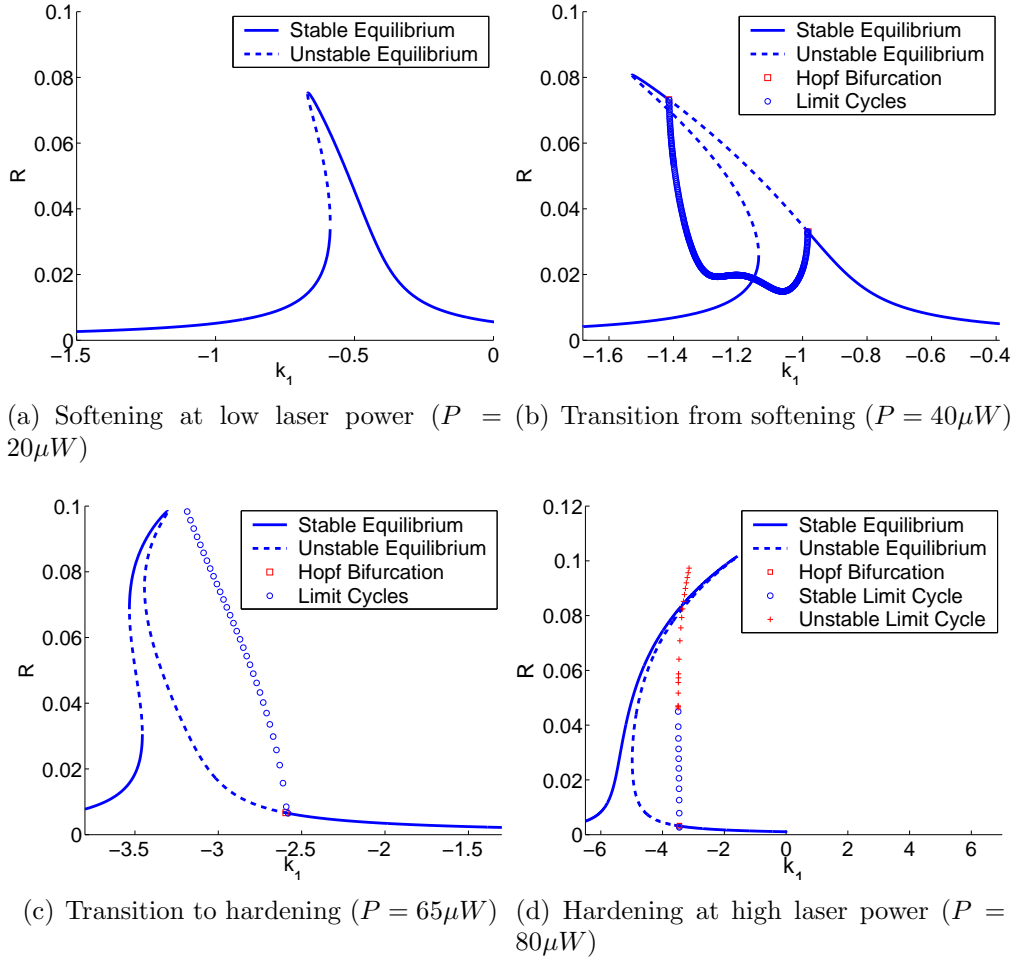
(d) Hardening at high laser power ($P = 80\mu W$)

Figure 5: Amplitude Solid lines denote stable equilibria, dotted lines denote unstable equilibria, open squares denote Hopf bifurcation points, and open circles denote stable limit cycles and + denotes unstable limit cycles.
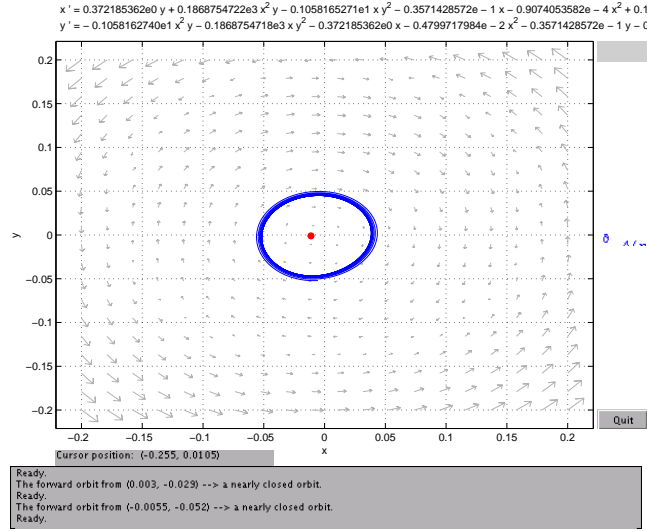
Figure 6: Phase portrait for $P = 65\mu W$ and $k_1 = -2.7$. The equilibrium in the center is unstable and the surrounding limit cycle is stable.
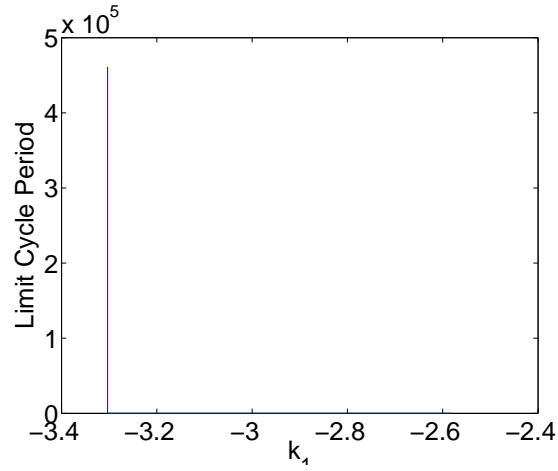
Figure 7: Time period of the limit cycle in Fig. 5(c). The growth of the time period suggests the existence of either a homo/heteroclinic or infinite period bifurcation.
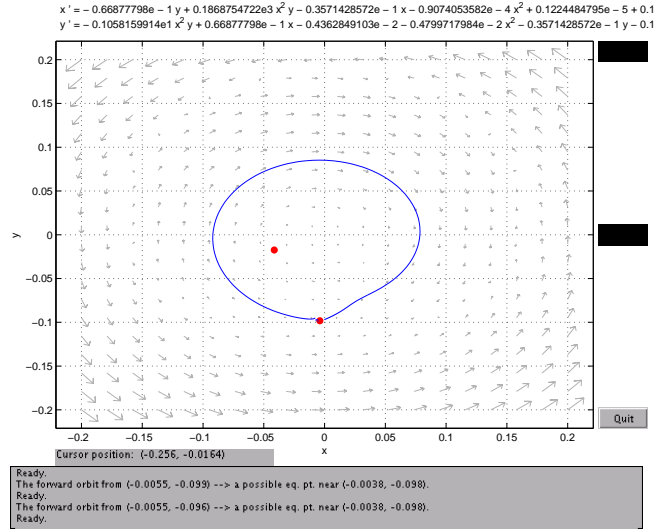
14

Figure 8: Phase portrait for $P = 65\mu W$ and $k_1 \approx -3.3$. The equilibrium in the center is unstable, the other equilibrium is right at the saddle node bifurcation that creates the stable and unstable equilibria. This trajectory comes about either due to a homoclinic or an infinite period bifurcation.
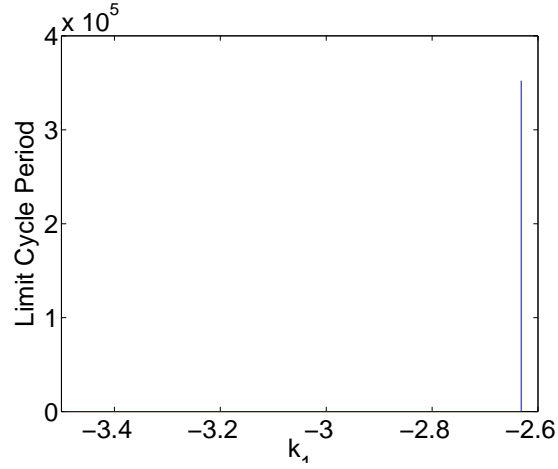

Figure 9: Time period of the limit cycle in Fig. 5(d). The growth of the time period suggests the existence of a homo/heteroclinic or infinite period bifurcation.
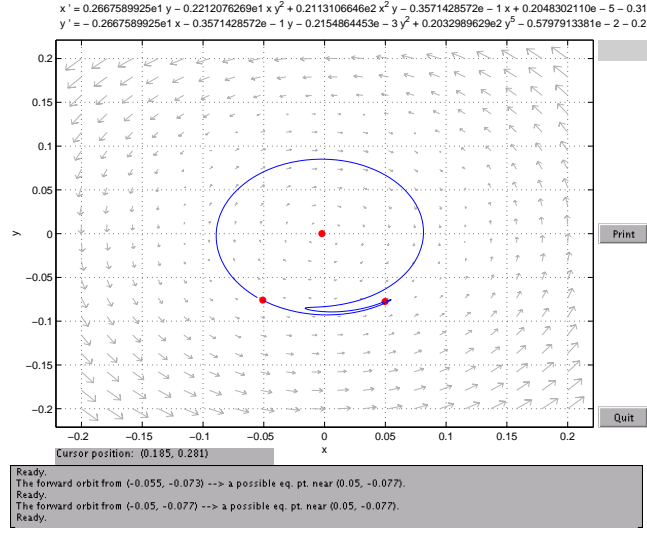
15

Figure 10: Phase portrait for $P = 80\mu W$ and $k_1 = -2.651794$. Connections exist between the saddle point and the stable node.

The main idea of the algorithm is encapsulated in Fig. 11. We take the "guess" torus (for a particular parameter value) integrate it forward by $\frac{2\pi}{\omega}$ and compute the "error" between the two curves. We then use Powell's hybrid method [30] to iterate the curve, until the computed "error" falls below a set tolerance. The algorithm steps are:

1. Start with a known initial curve in the Poincaré section.

2. Change parameter.

3. Using the last known curve as a guess, integrate the points on it for one Poincaré section giving a new curve.

4. Compute the "error" between the two curves.

5. Use an iterative scheme (e.g. Powell's hybrid method) to obtain the next guess.

6. Return to step 3 until "error" falls below accepted tolerance.

7. Treat new curve as initial guess for next parameter value

8. Return to step 2 until desired parameter value reached or convergence fails.

This gives us the curve that maps back onto itself in the Poincaré section at different parameter values (independent of the stability of the torus). The continuation algorithm is fairly straightforward. We have been a little vague about a couple of things, however. Namely, we have not explained how the initial "guess" is obtained, and how the "error" between the two curves is calculated.
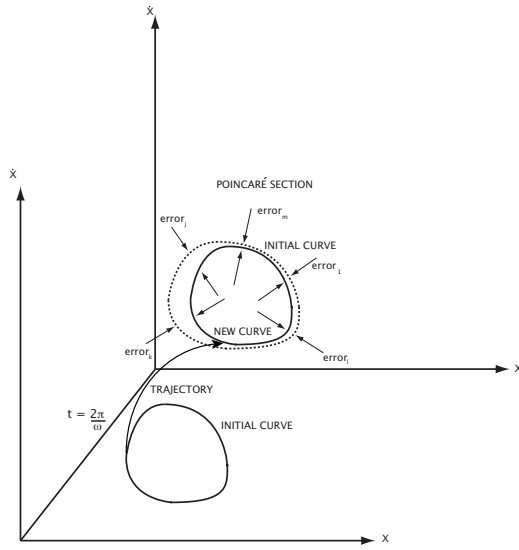
Figure 11: Schematic of algorithm to perform continuation of invariant tori.

One method to obtain the initial "guess" is to use simple numerical integration (see Figs. 13 and 14). Depending on the stability of the torus, the system may need to integrated either forwards (stable torus) or backwards (unstable torus). We then feed the curve in the Poincaré section (Fig. 14) into the iterative scheme, using the same parameter value as used for numerical integration. On convergence, we have a Poincaré section of the torus for a particular parameter value. We then change the parameter and use this computed torus as the initial guess for computation. To compute the error between curves (to be used by the iterative method) we use a cubic spline approach (see Fig. 12). The trouble is that the torus is represented by a linked list of marker particles. When these particles are integrated forward by $\frac{2\pi}{\omega}$ they need not fall exactly on top of the previous set of points, making computation of the error between the curves a little harder. Let C_1 be the last guess for the torus and C_2 be the computed curve, obtained by (forwards) integration (by $\frac{2\pi}{\omega}$) of all the marker particles that represent C_1. Let $P \in C_2$, we now want to compute the shortest distance between point P and curve C_1 (Fig. 12). To do this, we find the marker particle Q on C_1 that is closest to P. We then pass a natural cubic spline (the second derivatives at the ends are set to zero) through three closest neighbors to the "left" and three to the "right" (in a linked list nomenclature, denoted by red circles in Fig. 12) of Q. In this way we spline the part of C_1 closest to P. We then use a 1-D minimization routine (golden section minimization in our case [31]) to compute the arclength s_0 ($0 \leq s_0 \leq 1$) that minimizes the distance of P from the spline. The "error" is then set to the distance between this computed point on the spline at arclength s_0 and point P. This calculation is then repeated for all points that represent C_2.

The cubic spline places a requirement on the smoothness of the torus. Namely, we require that the torus remain C^2 (second derivative remains continuous). If the points representing the torus become too irregular (lose smoothness) the above algorithm fails.
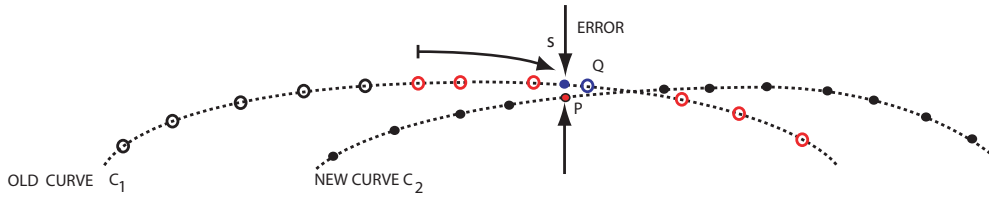
17

Figure 12: Method of computing the error between the last known torus and the new one.

3.1.1 Implementation

Before we go the the results, a few words about the implementation of the continuation algorithm. The code (written in C++) to perform continuation of invariant tori is built on top of GNU Scientific Library (GSL). This library is used to integrate the system of equations and perform the iterative scheme. The data structure used to store the curves is a circular linked list [32]. The Jacobian calculation is very rudimentary. We use finite differences (implemented within the library for Powell's Hybrid method) to compute the stability of the tori. A more sophisticated approach would be to use sensitivity matrices [33].

The distance between points on the torus is regulated by setting thresholds. If the distance between two neighboring points falls below a minimum prescribed threshold, one of points is deleted. Similarly, if the distance between two neighboring points increases beyond a maximum prescribed threshold, a new point is inserted between the two points using cubic spline interpolation.

3.2 Results

Quasiperiodic oscillations can be obtained by numerical integration, for example Figs. 13 and 14. These solutions serve as an initial guess for the continuation algorithm. Using these initial conditions, we can compute the family of invariant tori as shown in Figs. 15 and 16. It is important to note that the results shown in Figs. 15 and 16 are for $P = 65\mu W$ (corresponding to Fig. 2(d) and 3(d)). We see the same qualitative picture for $P = 60\mu W$. For $P = 22\mu W$, the picture is less interesting and the torus is just born at one torus bifurcation and dies at the other (explained in more detail later). For $P = 65\mu W$ (and $P = 60\mu W$) we find that, on decreasing ω, the torus begins to fold onto itself (see Figs. 15) resulting in torus breaking [24]. This suggests the presence of stable and unstable periodic orbits lying on the torus [34]. Folding may be a consequence of the interaction of the torus with the unstable manifold of the unstable periodic orbit (that lies on the torus) [34]. The study of torus breaking and related phenomena is a subject for future work. We now try to complete the phase portrait in the Poincaré map.

3.2.1 Computing Equilibria

It will be informative to overlay the locations of equilibria (in the Poincaré map, the equilibria correspond to periodic orbits in Figs. 2 and 3) on top of the tori in Figs. 15 and 16. We compute the equilibria by (once again) resorting to a Newton Raphson scheme. An initial
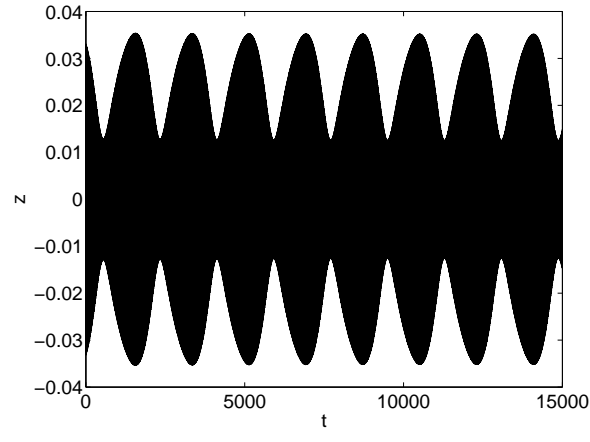
Figure 13: Quasiperiodic response of the oscillator at $P = 65\mu W$ and $\omega = 0.575$
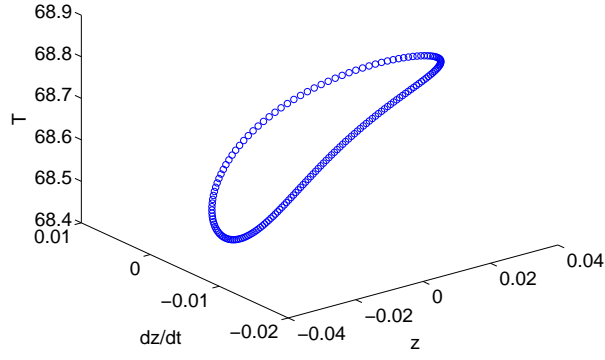

Figure 14: Poincaré section of quasiperiodic motion at $P = 65\mu W$ and $\omega = 0.575$. Obtained by strobing the system (Eqn. 1) at $t = \frac{2n\pi}{\omega}$ (n is an integer).
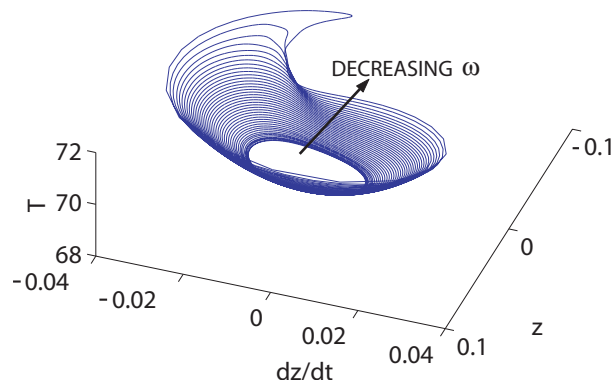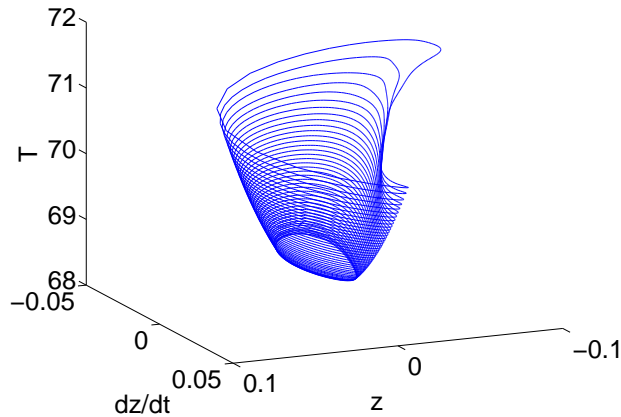

Figure 15: Family of tori with changing ω.

19

Figure 16: Family of tori with changing ω.

guess is picked in the vicinity of the expected equilibrium and then integrated for $t = \frac{2\pi}{\omega}$. The error between the new point and initial point is fed into the root finder (Newton Raphson scheme) to find the next guess for the point. We repeat this until the error falls below a prescribed tolerance. Fig. 17 shows the evolution of the torus for $P = 65\mu W$ with respect to equilibria (periodic solutions in Figs. 2 and 3) in the Poincaré section.

To get a measure of the vector field around the torus, we evolve a small line segment (represented only by two end points) in the vicinity of the stable equilibria (of the map), backwards in time. The small segment is chosen to be orthogonal to the eigendirection corresponding to the largest Floquet multiplier. These segments in effect become an approximation to a subset of the stable manifold of the equilibrium.

We find that in the vicinity of the fold of the torus, the line segments turn away from the fold (see Figs. 18 and 19). This demonstrates large changes in the vector field in the region around the fold. These segments may be interacting with the unstable manifold of the unstable periodic orbits on the torus [34]. Now that we have the results from continuation, we can predict jump and drop locations, and (hence) hysteresis present in the system (the locations of torus breaking match the results from numerical integration shown in Fig. 2 and 3).

4   Conclusions

In the first part of this paper we used perturbation theory to derive equations for the dynamics of the oscillator in the Poincaré section by using the method of multiple scales to $O(\epsilon)$. This approach captured the softening hardening transition (see Fig. 4) but not the torus bifurcations in Fig. 2. This forced us to go to $O(\epsilon^2)$. The higher order method is found to give significantly better results. It recreated the exact backbone transitions in Fig. 2 along with the torus (Hopf in the slow flow) bifurcations (shown in Fig. 5). The limit cycles (in the slow flow) that emerge from the (slow flow) Hopf bifurcation are tracked. We find that that for lower laser powers the limit cycles are born at a Hopf bifurcation and die at a Hopf
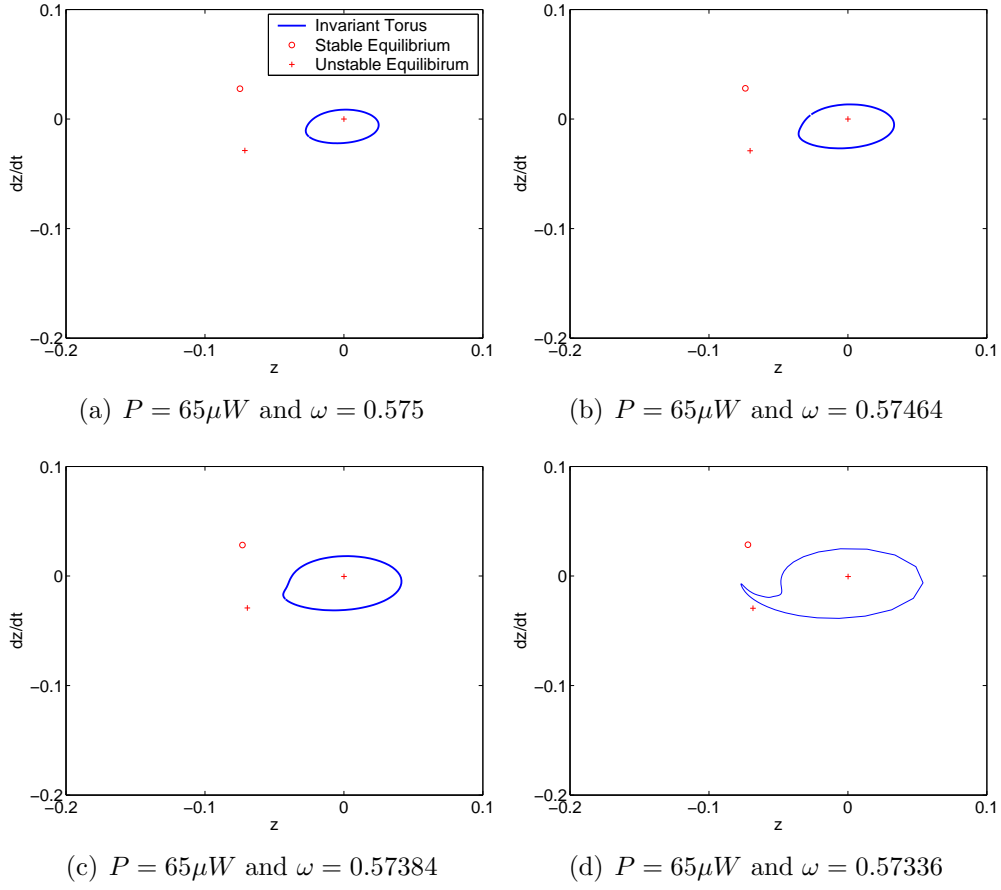
(a) $P = 65\mu W$ and $\omega = 0.575$ (b) $P = 65\mu W$ and $\omega = 0.57464$

(c) $P = 65\mu W$ and $\omega = 0.57384$ (d) $P = 65\mu W$ and $\omega = 0.57336$

Figure 17: The torus plotted with respect to the equilibria at various parameter values .
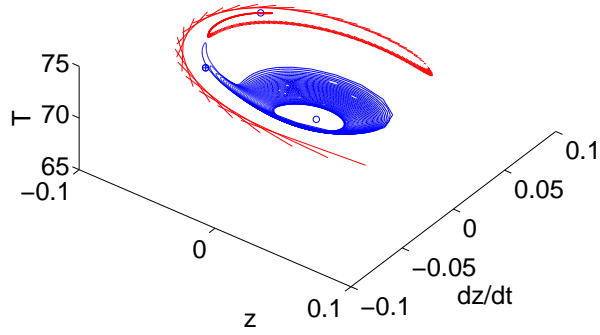

Figure 18: Family of tori with changing ω plotted with the equilibrium and a subset of the stable manifold of the stable equilibrium
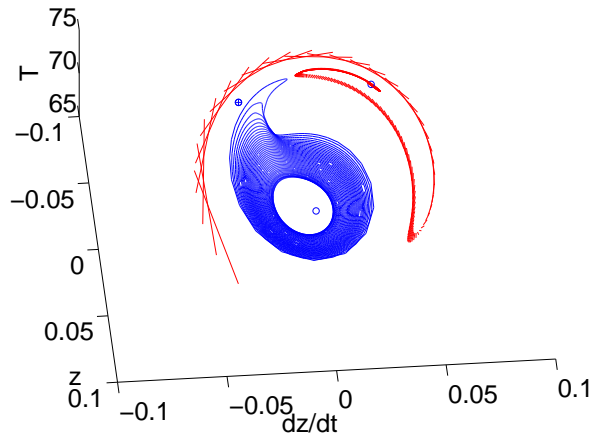
Figure 19: Family of tori with changing ω plotted with the equilibrium and a subset of the stable manifold of the stable equilibrium

bifurcation Fig. 5(b). For higher laser powers the limit cycles meet their deaths at an infinite period bifurcation (see Figs. 5(c) and 5(d)). This result is found not to match numerical integration. This is probably due to application of the method of multiple scales beyond the range of validity [21].

In the second part we implemented a continuation algorithm to compute the branch of invariant tori in Fig. 2 and 3. Using this numerical scheme we get an answer that matches the results from numerical integration shown in [15] (in Fig. 2). The torus breaks due to the stretching along directions associated with unstable manifolds of periodic orbits on the torus [34].

5   Acknowledgments

References

[1] J. S. Aldridge and A. N. Cleland. Noise-enabled precision measurements of a Duffing nanomechanical resonator. *Physical Review Letters*, 94:156403, 2005.

[2] B. Ilic, H.G. Craighead D. Czaplewski, P. Neuzil, C. Campagnolo, and C. Batt. Mechanical resonant immunospecific biological detector. *Applied Physics Letters*, 77:450–452, 2000.

[3] K.L. Ekinci, X.M.H. Huang, and M.L. Roukes. Ultrasensitive nanoelectromechanical mass detection. *Applied Physics Letters*, 84(22):223–256, 2004.

[4] A.N. Cleland and M. L. Roukes. A nanometre-scale mechanical electrometer. *Nature*, 392:160–162, 1998.

[5] R.B. Reichenbach, M. Zalalutdinov, K.L. Aubin, R. Rand, B. Houston, J.M. Parpia, and H.G. Craighead. 3rd order intermodulation in a micromechanical thermal mixer. *Journal of Microelectromechanical Systems*, 14(6):1244–1252, 2005.

[6] S. Lee, M.U. Demirci, and C.T.C. Nguyen. A 10-MHz micromechanical resonator Pierce reference oscillator for communications. In *Digest of Technical Papers, the 11th International Conference on Solid-State Sensors and Actuators (Transducers 01)*, pages 1094–1097, 2001.

[7] F.C. Hoppensteadt and E. M. Izhikevich. Synchronization of mems resonators and mechanical neurocomputing. *IEEE Transactions on Circuits and Systems–I: Fundamental Theory and Applications*, 48(2):133–138, 2001.

[8] T. Sahai and A. T. Zehnder. Modeling of coupled dome-shaped micro-oscillators. *IEEE/ASME Journal of Micro-Electro-Mechanical Systems*, 17(3):777–786, 2008.

[9] K.L. Turner, S.A. Miller, P.G. Hartwell, N.C. MacDonald, S.H. Strogatz, and S.G. Adams. Five parametric resonances in a microelectromechanical system. *Nature*, 396:149–152, 1998.

[10] M.F. Yu and et al. Realization of parametric resonances in a nanowire mechanical system with nanomanipulation inside a scanning electron microscope. *Physical Review B*, 66:073406, 2002.

[11] K. Aubin, M. Zalalutdinov, T. Alan, R. Reichenbach, R. Rand, A. Zehnder, J. Parpia, and H. Craighead. Limit cycle oscillations in cw laser driven nems. *Journal of Microelectromechanical Systems*, 13(6):1018–1026, 2004.

[12] M. Zalalutdinov, K.L. Aubin, M. Pandey, A.T. Zehnder, R.H. Rand, H.G. Craighead, and J.M. Parpia. Frequency entrainment for micromechanical oscillator. *Applied Physics Letters*, 83(16):3281–3283, 2003.

[13] V. Kaajakari and A. Lal. Parametric excitation of circular micromachined polycrystalline silicon disks. *Applied Physics Letters*, 85(17):3923–3925, 2004.

[14] X. Zhao, H. Dankowicz, C.K. Reddy, and A.H. Nayfeh. Modeling and simulation methodology for impact microactuators. *Journal of Micromechanics and Microengineering*, 14:775–784, 2004.

[15] T. Sahai, R. Bhiladvala, and A. Zehnder. Thermomechanical transitions in doubly-clamped micro-oscillators. *International Journal of Nonlinear Mechanics*, 42(4):596–607, 2007.

[16] E.J. Doedel, H.B. Keller, and J.P. Kernevez. Numerical Analysis and Control of Bifurcation Problems, Part I. *International Journal of Bifurcation and Chaos*, 1(3):493–520, 1991.

[17] E.J. Doedel, H.B. Keller, and J.P. Kernevez. Numerical Analysis and Control of Bifurcation Problems, Part II. *International Journal of Bifurcation and Chaos*, 1(4):745–772, 1991.

[18] R. Rand. *Lecture Notes on Nonlinear Vibrations*. Cornell University, available at http://www.tam.cornell.edu/randdocs/, 2003.

[19] A. Nayfeh. *Perturbation Methods*. Wiley Publishers, first edition, 1973.

[20] J. Kevorkian and J. D. Cole. *Multiple Scale and Singular Perturbation Methods*. Springer, first edition, 1996.

[21] A. H. Nayfeh. Resolving controversies in the application of the method of multiple scales and the generalized method of averaging. *Nonlinear Dynamics*, 40:61–102, 2005.

[22] A. Nayfeh and D. Mook. *Nonlinear Oscillations*. Wiley Publishers, first edition, 1979.

[23] S. L. Das and A. Chatterjee. Multiple scales without center manifold reduction for delay differential equations near hopf bifurcations. *Nonlinear Dynamics*, 30(4):323–335, 2002.

[24] J. Guckenheimer and P. Holmes. *Nonlinear Oscillations, Dynamical Systems and Bifurcations of Vector Fields*. Springer, New York, 1996.

[25] L. O. Chua and A. Ushida. Algorithms for computing almost periodic steady-state response of nonlinear systems to multiple input frequencies. *IEEE Transactions of Circuits and Systems*, 28(10):953–971, 1981.

[26] C. Díez, À Jorba, and C. Simó. A dynamical equivalent to the equilateral libration points of the real earth-moon system. *Celestial Mechanics*, 50(1):13–29, 1991.

[27] F. Schilder, H. M. Osinga, and W. Vogt. Continuation of quasi-periodic invariant tori. *SIAM Journal on Applied Dynamical Systems*, 4(3):459–488, 2005.

[28] E. J. Doedel, T. F. Fairgrieve A. R. Champneys, Y. A. Kuznetsove, B. Sandstede, and X. Wang. Auto 97: Continuation and bifurcation software for ordinary differential equations (with homcont). *AUTO97 Manual*, 1997.

[29] I. G. Kevrekidis, R. Aris, L. D. Schmidt, and S. Pelikan. Numerical computation of invariant circle of maps. *Physica D*, 16(2):243–251, 1985.

[30] P. Rabinowitz. *Numerical Methods for Nonlinear Algebraic Equations*. Gordon and Breach Science Publishers, 1970.

[31] R. P. Brent. *Algorithms for minimization without derivatives.* Englewood Cliffs, New Jersey: Prentice Hall, 1975.

[32] D. Knuth. *The Art of Computer Programming Vol I.* Addison-Wesley, second edition, 1973.

[33] E. A. Coddington and N. Levinson. *Theory of Ordinary Differential Equations.* McGraw-Hill, first edition, 1955.

[34] D. G. Aronson, M. A. Chory, G. R. Hall, and R. P. McGehee. Bifurcations from an invariant circle for two-parameter families of maps of the plane: A computer-assisted study. *Communications in Mathematical Physics*, 83(3):303–354, 1982.